Inhibition of hydrogen and oxygen recombination over amide–functionalized graphene and the enhancement of photocatalytic hydrogen generation in dye–sensitized AF–RGO/Pt photocatalyst dispersion

Xuqiang Zhang[a], Dan Luo[b], Wenyan Zhang[a,c,d], Wei Gao[a,c], Xiaofeng Ning[a,c], Hongxia Liu[a,c], Bin Tian[a,c], Baojun Yang[a,*], Gongxuan Lu[a,*]

[a] State Key Laboratory for Oxo Synthesis and Selective Oxidation Lanzhou Institute of Chemical Physics, Chinese Academy of Science, Lanzhou, 730000, China
[b] College of Physics & Electronic Engineering, Northwest Normal University, Lanzhou, 730070, China
[c] University of Chinese Academy of Science, Beijing, 100049, China
[d] College of Material Engineering, Jinling Institute of Technology, Nanjing, China

ARTICLE INFO

ABSTRACT

Photocatalytic hydrogen evolution (PHE) is a promising way to generate hydrogen driven by solar light. Noble metallic Pt is usually used as a co–catalyst to catalyze this reaction. However, Pt can also act as an active center for H_2 and O_2 recombination reverse reaction, which results in the low photocatalytic efficiency for H_2 generation. Herein, the H_2 and O_2 recombination can remarkably be inhibited by incorporating amide–functionalized groups onto graphene surface and edge, which act as the oxygen adsorbent site and reduce migration of O_2 molecules in the dye–sensitized PHE system. Theoretical studies verify that the adsorption energy of oxygen change remarkable due to orbital hybridization by N 2p in amide group with O 2p in O_2 molecule, leading to redistribution the electron structure of graphene, and change of electrical properties of sensitized matrix. By amide–functionalized graphene (AF–RGO), we achieved high H_2 evolution activity over AF–RGO/Pt nanohybrid catalyst under visible light irradiation. The quantum efficiency of AF–RGO/Pt (AF–RGO prepared at 140 °C) achieved 36.4% at 430 nm. This superior photocatalytic performance can be attributed to the repression of H_2 and O_2 recombination and the synergy of electrical properties. This work is helpful to design high active catalyst for solar hydrogen generation.

1. Introduction

The dye–sensitized photocatalytic hydrogen evolution (PHE) from water reduction is an important route for solar light store and conversion because these systems absorb longer wavelength visible light that comprises a majority of the solar spectrum [1–17]. Commonly, a dye–sensitized catalyst for PHE is composed of a light–absorbing dye, sensitized matrix and co–catalyst. An excellent co–catalyst can work as highly active sites to reduce the overpotential of hydrogen evolution [13,15]. Noble metal (Pt and Pd) co–catalysts show the high activity for the generation of hydrogen [18–24], however, they can also catalyze hydrogen and oxygen recombination back to water [25–32]. Actually, hydrogen and oxygen recombination can easy occur over noble metal loaded catalysts at room temperature and has been widely used in hydrogen removal passive autocatalytic recombiner to avoid the explosion risk in water–cooled nuclear reactors and submarines under normal and emergency operating conditions [27,28].

In many cases, hydrogen and oxygen coexist and dissolve in the liquid water. It is known that more oxygen can be dissolved in water then hydrogen under same conditions [25,26]. Therefore, the nascent formed hydrogen will be consumed severely by dissolved oxygen due to spontaneous inverse hydrogen and oxygen recombination on the co–catalyst surface, which will seriously impede the over–all hydrogen generation rate during photocatalytic water splitting. Several strategies have been reported to inhibit this recombination in the PHE [25,26,29–32]. For example, the higher oxidation state Pt can markedly inhibit the recombination of hydrogen and oxygen, while its hydrogen evolution capacity is still remained compared to that of conventional metallic Pt cocatalyst [29]. Zhu et al. [30] also found that the formaldehyde oxidation activities over halogen–adsorbed Pt–TiO₂ catalyst could be significantly reduced due to the stronger Pt–X bond, which decreased the adsorption and activation of oxygen on the Pt surface. Recently, Kang et al. [31] reported that the ternary doping of F into SrTiO₃:Cr/Ta could increase the hydrogen evolution rate under visible

light irradiation due to F–SrTiO$_3$ interaction. Our previous work reported that the backward reaction of hydrogen–oxygen recombination was successfully restrained by addition of oxygen transfer reagent hemin chloride in the Pt/TiO$_2$ catalytic system [26]. We also found that the trace amount of fluorine ion could also remarkably inhibit hydrogen and oxygen recombination due to occupation of hydrogen and oxygen adsorption and activation sites by fluorine ion occupation on Pt sites [25]. Although H$_2$ and O$_2$ recombination reaction in PHE is well acknowledged, the controllable inhibition of oxygen adsorption and activation over catalyst is still challenging due to lacking of strategy and materials which exhibit tunable oxygen activation over catalyst.

Herein, the solvothermal preparation amide–functionalized graphene oxide (AF–RGO) matrix shows significant inhibition properties for H$_2$ and O$_2$ recombination reaction. It is confirmed that the amide functionalized groups over GO can effectively inhibit H$_2$ and O$_2$ recombination by decrease of adsorption dissolved oxygen by the enhancement of hydrophobicity properties of catalyst in water and variation of electrical properties of catalyst by the amide functionalized groups, as a result, the adsorption of O$_2$ in the solution is remarkably reduced. The calculation results indicate adsorption energy changes significantly after the amide functionalization, which leads to the decrease of hydrogen and oxygen recombination. The AF–RGO/Pt nanohybrid catalyst displayed highly efficient dye–sensitized photocatalytic H$_2$ evolution under the visible irradiation and the quantum efficiency achieved 36.4% at 430 nm. Results in this paper might light the possible route to build up active photocatalyst for dye–sensitized PHE from water.

2. Experimental section

2.1. Preparation of AF–RGO

GO was synthesized by the oxidation of high purity graphite powder according to the modified Hummers' method [15,32]. The synthesized GO (100 mg) was dispersed in the DMF (100 mL) by ultrasound dissolving, which acted as a dispersing, reducing and stabilizing agent. Then, a small amount of de–ionized water was added into the resulting dispersion above. After being stirred for a few minutes, the obtained yellow brown dispersion of GO was placed into a two–necked, round–bottomed flask and heated to a set temperature (80, 100, 120 and 140 °C, respectively) for 12 h under Ar atmosphere in an oil bath under magnetic stirring and refluxing. After that, the reaction system was cooled to room temperature, and a different degrees of black colloid dispersion was separated from the suspension by suction filtration on the organic filtration membrane and repeatedly washed with ethanol and de–ionized water several times to remove residue of DMF. It was worth noting that the system smelled an intense odor of amine from the dispersion after the reaction. The final products were dried in an oven at 30 °C for 10 h, and ground to obtain AF–RGO, which were denoted as T:AF–RGO, where T describes the treatment temperature (T = 80, 100, 120 and 140 °C, respectively). A schematic illustration of the experimental process was shown in Scheme 1. For comparison, the bare GO has not been heat treated in the DMF, and it only disperses in DMF at room temperature.

2.2. Preparation of T: AF–RGO/Pt and measurement of catalyst activity

Synthesis of T:AF–RGO/Pt photocatalysts and activity measurements were performed in a sealed Pyrex flask (200 mL) with a flat window (an efficient irradiation area of 13.2 cm^2) and a silicone rubber septum for sampling at ambient environment. Highly active H$_2$ evolution T:AF–RGO/Pt (T = 80, 100, 120 and 140 °C, respectively) photocatalysts systems were prepared by an in situ photo–deposition method. 5.0 mL of the T:AF–RGO suspensions aqueous solution (1.0 mg/mL) and 500 μL of aqueous K$_2$PtCl$_6$ (5.0 mg/mL) were dispersed in 100 mL of triethanolamine solution (TEOA/H$_2$O, pH = 7.0, 10% (v/v)), and the
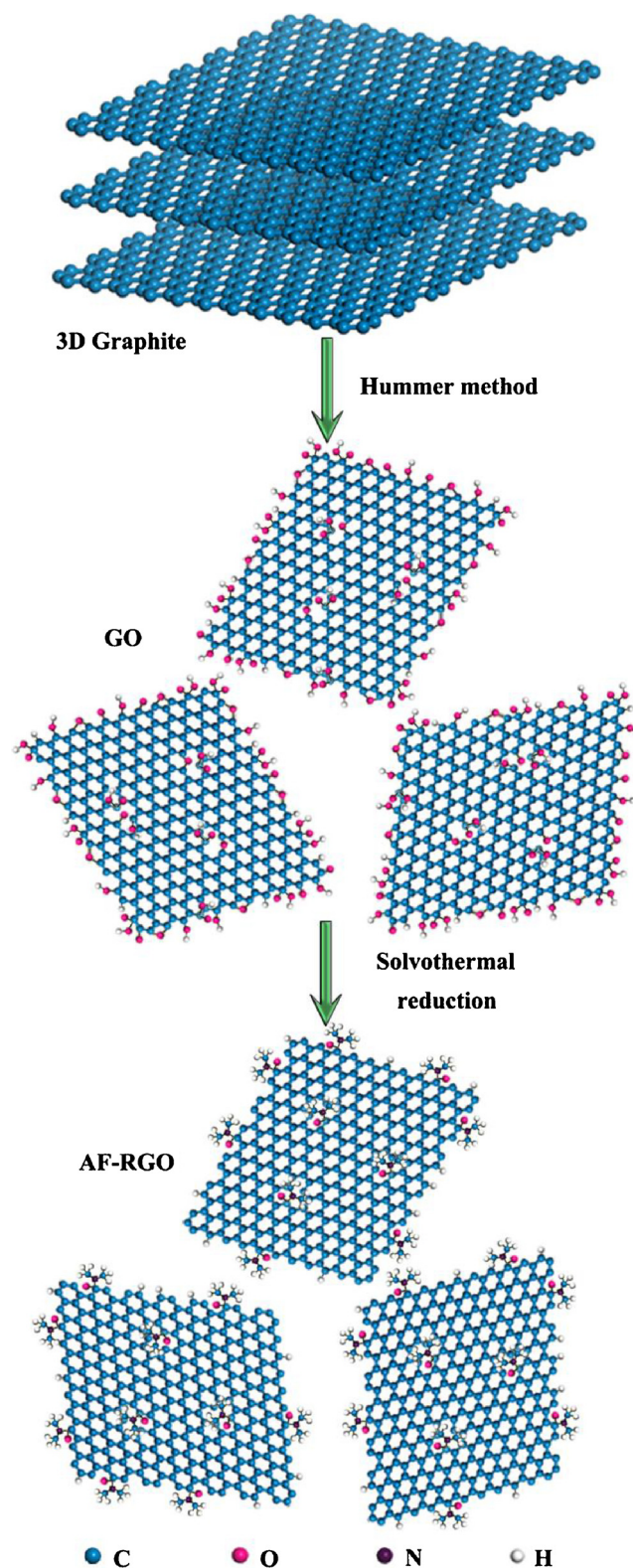
Scheme 1. Schematic diagram depiction the preparation of GO by the oxidation of high purity graphite powder according to the modified Hummers' method, and AF–RGO by solvothermal treatment GO in DMF as a dispersing, reducing and stabilizing agent at 80, 100, 120 and 140 °C, respectively.

pH value of reaction resolution was adjusted by hydrochloric acid or sodium hydroxide solution. Then, 35 mg of the Eosin Y (EY) was added in the mixed solution. Prior to irradiation, the suspension mixture was dispersed by ultrasonic treatment for 30 min and degassed by bubbling

Ar gas for 20 min. The mixed dispersion was irradiated by visible light, which was equipped with either a 420 nm cutoff filter or various band–pass filters, and the light source was a 300–W Xe lamp. The amount of hydrogen evolution was measured using gas chromatography (Agilent 6820, TCD, 13 × column, Ar carrier). For comparison, the Pt nanoparticles (NPs) were synthesized under the same conditions without adding T:AF–RGO suspensions.

2.3. Recombination experiments of hydrogen and oxygen

The recombination experiments of hydrogen and oxygen was carried out in the same sealed Pyrex flask and a silicone rubber septum for sampling. The details of the experiments were as follows. The centrifugal and dried T:AF–RGO/Pt catalyst was dispersed into 100 mL of de–ionized water and was treated with the ultrasound about 15 min to make the catalyst dispersed well. Subsequently, the suspension was degassed by bubbling Ar gas for 30 min to exclude the air inside. After that, 1 mL H_2 and 1 mL O_2 were injected into the reactor to conduct the hydrogen and oxygen recombination reaction. The recombination rate of hydrogen and oxygen was measured by detection of decreased amount of hydrogen using gas chromatography.

2.4. Apparent quantum efficiency (AQE) for hydrogen evolution and stability measurements of catalysts

The AQE of catalyst for hydrogen evolution was measured under light irradiation through a band–pass filter (420, 460, 490, 520, or 550 nm respectively). T:AF–RGO (1.0 mg/mL × 5.0 mL) nanohybrid was dispersed in TEOA aqueous solution (100 mL, pH = 7, 10% (v/v)), and then Eosin Y (35 mg) and K_2PtCl_6 (5.0 mg/mL × 0.5 μL) were added. The reactant mixture was degassed by bubbling Ar gas for 30 min, and then was irradiated by a 300–W Xe lamp with a cutoff filter for 20 min. After that, the reaction system was degassed again by bubbling Ar gas. The reaction solutions were re–irradiated for 20 min with another band–pass filters for AQE for H_2 production. The AQE was calculated with the following equation:

$$AQE[\%] = \frac{2n_{H_2}}{N_P} \times 100\% \tag{1}$$

where $2n_{H_2}$ and N_P represents the number of reacted electrons during hydrogen evolution and the number of incident photons in the entire reaction process, respectively. Photon flux of the incident light was determined using a Ray virtual radiation actinometer (FU 100, silicon ray detector, light spectrum, 400–700 nm; sensitivity, 10–50 μV μmol^{-1} m^{-2} s^{-1}). The stability tests were carried out for 120 min (four runs) under visible light; after the first run of 120 min, the catalyst was separated by centrifugal method. After washing thoroughly by deionized water, the catalysts were mixed with TEOA solution and fresh EY in the same way.

More details, including chemical reagent and working electrode preparation, electrochemical measurements and specimen characterization, were stated in the Supporting information.

3. Results and discussion

3.1. Structure and morphology characterizations

In order to study the variation of functional groups on the surface of samples after solvothermal treatment, the Fourier transform infrared spectra (FTIR) experiments are executed and analyzed. From the FTIR spectra of bare GO and T:AF–RGO in the Fig. 1a, it can be observed that the samples exhibit several characteristic absorption bands of oxygen containing groups. The peaks at 1076 and 1282 cm^{-1} are attributed to C−O and C−O−C stretching modes, respectively. The C=C skeleton vibration peak can be observed around 1641 cm^{-1} and the IR absorption at about 1728 cm^{-1} is assigned to the C=O stretching vibration. The

intense peak by C−H stretching vibrations is at about 2958 cm^{-1} [11,33]. The broad peak in the range of 3000–3500 cm^{-1} is attributed to the O−H stretching vibrations of the C−OH groups. Noted that the absorption peak of most oxygen containing groups decreased or even disappeared after the solvothermal treatment, which indicated the occurrence of the deoxygenation of GO. Moreover, the FTIR spectra of T:AF–RGO, as compared to GO alone, showed an additional absorption around ~1376–1385 cm^{-1} indicating the probably newly formed C−N bonding on GO [33]. And the intensity of absorption peak gradually enhanced with the increase of treatment temperature, and becomes relatively stronger with the increase of solvothermal temperature in Fig. 1b. indicating plenty of nitrogen–containing functional groups were introduced in graphene surface. It is worth noting that the C−N bonding locates at ~1388 cm^{-1} from DMF and shifts toward lower wavenumber. These results indicate that the C−N bond is formed and connected with AF–RGO.

In order to further investigate the effect of surface functional group variation, water contact angle of samples was measured. Contact angle reflects the wettability of a solid surface and can be used to determine the adhesion force between a drop and solid surface [15,34]. Here, the values of contact angle are obtained by measuring with 5 mL water droplets at five different positions on each sample and the optical pictures are obtained by a digital camera under the room temperature. The water contact angles θ of T:AF–RGO increase with solvothermal temperatures from 64.47° to 84.92°, which are higher than that of the bare GO (θ = 62.61), as shown in Fig. 2. These results indicate the T:AF–RGO has lower surface energy compared with bare GO [34], which corresponds the surface group variation indicated in FTIR spectra. In other words, the hydrophobic groups on the surface of T:AF–RGO can decrease the interaction between dissolved oxygen with photocatalyst, as a result, the reverse recombination of hydrogen and oxygen can be inhibited. Interestingly, compared with the contact angle of reduced GO (96.53°) by N_2H_4 solution at 90 °C, the T:AF–RGO still remains hydrophilic properties (0° ≤ θ ≤ 90°), which makes catalyst dispersing well in water.

In order to study the chemical states of elements in catalyst, the XPS spectra were measured. The survey XPS spectra of samples (see Fig. S1) showed typical C1 s, O1 s and N1 s peaks, no other peaks of impurities appeared. Fig. 3a–e presented the deconvoluted C1 s spectra of bare GO and T:AF–RGO, which identified the functional group variation. The peak at 284.6 ~ 284.8 eV could be assigned to the C=C and the peaks at 285.6–285.8, 286.9–287.3 and 288.2–288.3 eV could be assigned to the C−N, C−O−C and O−C=O groups, respectively [3,25,33,38,47]. In the case of bare GO, the intensities of the C−O−C and O−C=O peaks were high, however, a noticeable decrease in the intensity of these peaks could be observed after solvothermal treatment. The carboxyl groups of T:AF–RGO are relatively high compared with others functional groups, however, the oxygen content of T:AF–RGO gradually decrease with the increase of temperature compared with bare GO. Moreover, the C−N peak only appeared in the T:AF–RGO sample, and their peak intensities became stronger with the increase of reaction temperatures. An atomic ratios of nitrogen are about 1.42, 2.16, 2.72 and 2.86 at.% in the several T:AF–RGO samples treated at different reaction temperatures (see Fig. 3f). These results indicated that the solvothermal treatment made GO incorporate with nitrogen atoms or nitrogen–containing functional groups into graphene surface, and significantly reduced the oxygen--containing functional groups over the surface of GO, as a result, the electrical properties and surface energy of graphene decreased. Moreover, after solvothermal treatment, the C1 s of 140:AF-RGO shows only one predominant peak at 284.7 eV (Fig. 3e), which can be attributed to graphitic carbon systems, and the tail of this signal at high binding energy indicates that there are still a certain amount of carbon atoms covalently bound with oxygen remaining in the AF-RGO.

Bare GO only possesses two main peaks in the XRD pattern, as shown in Fig. 4a, the sharp peak at 2θ = 10.05° indicates the highly crystalized structure with an interlayer spacing of 0.879 nm, which is
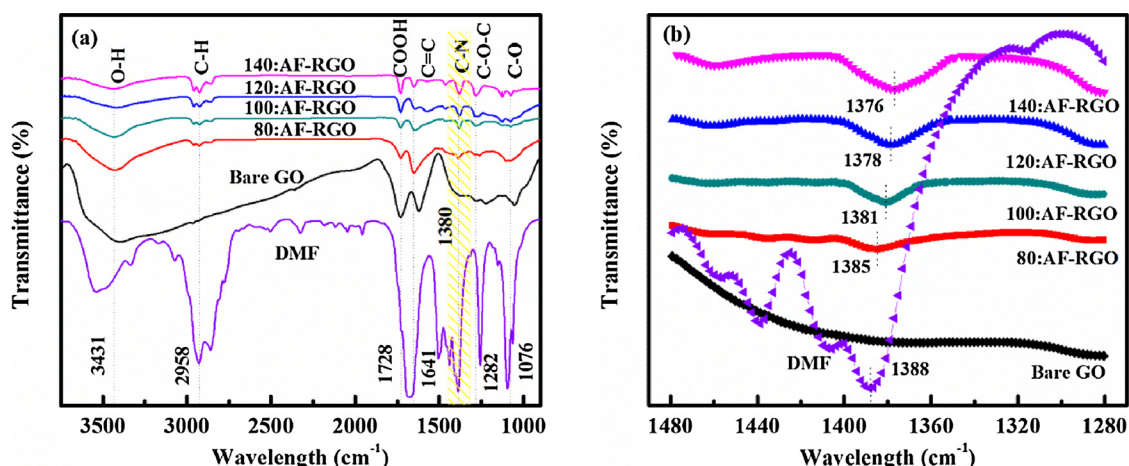
Fig. 1. (a) FTIR spectra of DMF, bare GO and T:AF–RGO (T = 80, 100, 120 and 140 °C), respectively. (b) The magnified window showing the C−N bonding of specimens.

typical characteristics of introduction of oxygen–containing groups into the crystal lattice during the oxidation process of graphite [5,15]. Another peak at 2θ = 20.09°, corresponding to a d–spacing of 0.441 nm, is indicative of a lower degree of crystallization and the presence of some defects in graphene [15,36]. Compared with bare GO, the diffraction peaks of T:AF–RGO obviously shift toward higher diffraction angles and become relatively stronger with the increase of reaction temperature from 80 to 140 °C (Figs. 4a and S2). Furthermore, the intensity and the full widths at half–maximum of the diffraction peaks also become weaken and broaden, respectively. This means that the interlayer spacing of T:AF–RGO decreases from 0.879 nm of the bare GO to 0.370 nm in 140:AF–RGO. These gradually decrease of interlayer spacing values confirm the decomposition of the GO sheets to graphene sheets, and a large amount of oxygen–containing groups are removed [15,37], nevertheless, the basal spacing is higher than that of well–ordered graphite (d_{002} = 0.335 nm) [38]. That higher basal spacing may be due to the presence of residual and new functional group from incomplete reaction of GO sheets to graphene. Moreover, the broad diffraction peaks of T:AF–RGO indicate that the samples are poorly ordered along the stacking direction [32,37].

Raman spectra of catalyst samples are shown in Fig. 4. As shown in Fig. 4b, both bare GO and T:AF–RGO show two distinct peaks of D band (∼1353.2 cm^{-1}) and G band (∼1595.7 cm^{-1}), as well as a weak 2D band (∼2951.2 cm^{-1}), which are the characteristic peaks of graphene [3,31,33,34,39]. It is worth noting that the D/G intensity ratios (I_D/I_G) of T:AF–RGO samples are 0.917, 0.920, 0.959 and 0.987 treated at reaction temperatures of 80, 100, 120, and 140 °C, respectively (shown in Fig. S3), which are higher than that of bare GO (0.884). This means that the carbon lattice structure of T:AF–RGO is highly disordered, and this disorder tendency increases with the increase of treat reaction temperature due to the cracking and edge distortion during the treatment progress. The disordered structures in the T:AF–RGO could increase platinum binding sites [15]. Moreover, a weaker and less distinct 2D band of T:AF–RGO than the bare GO is observed, which implies the disorder–induced D band and less layer number in catalyst obtained by solvothermal treatment [32,39].

The color of dispersion changes from yellow brown into deep black after solvothermal temperature, as shown in Fig. S4. The as–prepared T:AF–RGO dispersion does not aggregate after more than one month storage and shows good stability. From the FESEM and TEM images (Figs. S5 and S6), we can clearly observe the curled and overlapped nanosheets structure in these samples. The 140:AF–RGO exhibits typical corrugations and scrolling characteristics due to solvothermal reduction [35,37,40], while the two–dimensional structure is maintained in T:AF–RGO. The same results can be achieved by

HAADF–STEM images, as shown in Fig. 5a and e. Compared with bare GO, the light belt of 140:AF–RGO is typical curl and wrinkle structure. Elemental mappings of the bare GO and 140:AF–RGO reveal that the C and O elements are relatively homogeneous distributed in the samples (see Fig. 5). Nitrogen heteroatom in 140:AF–RGO is also homogeneously distributed over the whole graphene sheet (Fig. 5i), indicating solvothermal treatment GO in DMF can make nitrogen–containing functional groups combining on to GO.

$$(2)$$

$$(3)$$
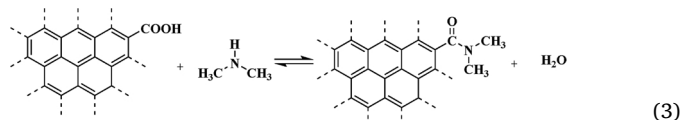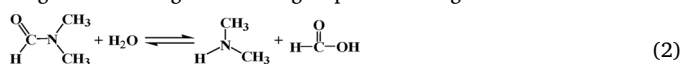
As reactions shown in the (2) and (3), DMF can be hydrolyzed into HCOOH and NH(CH$_3$)$_2$ (reaction (2)) [35,41,42], then the NH(CH$_3$)$_2$ can react with the –COOH on the AF–RGO edges by dehydration reaction and form amide functional groups [43,44]. The Ni 1 s XPS peak at 400 eV confirmed this reaction. Besides, the peak at 285.6 eV identified the formation of C−N in the −CON(CH$_3$)$_2$. These XPS results were supported by FTIR spectra of C−N bond in the T:AF–RGO. The amide groups modified on the edges of T:AF–RGO sheets can stabilize the T:AF–RGO sheets and enhance the catalyst dispersion ability in water. The dehydration reaction of hydroxyl and epoxy group leads to π–conjugation in graphene sheet of catalyst. Due to weak reducing ability of DMF [35,41,42], the reaction undergoes faster at higher temperature.

3.2. Electrical properties testing

Fig. 6 shows the I–V curves of the catalyst samples and gives their conductivity properties. Obviously, the current of 140:AF–RGO is about six orders of magnitude higher than that of bare GO. In addition, the conductivity of T:AF–RGO gradually increase with the increase of the treatment temperature. Since the oxygen–functionalized graphene sheet consists some hydroxyl and epoxy groups on the basal plane and carboxyl at the sheet edges, with a typical mixed sp^2–sp^3 hybridized phase, that bare sp^2 graphitic domains are well divided by small oxidized sp^3 fragments corresponding to hydroxyl, epoxy and carbonyl groups [11]. The conductivity of GO is comparatively poor to graphene, therefore, the current curve of bare GO has a drastic change when the voltage sweeps are in the range of −1.6 to 1.0 V due to high–resistance in the GO. Increasing the scanning voltage to higher side, the I–V curve of GO become stable and smoothness, but current is still low. Moreover,
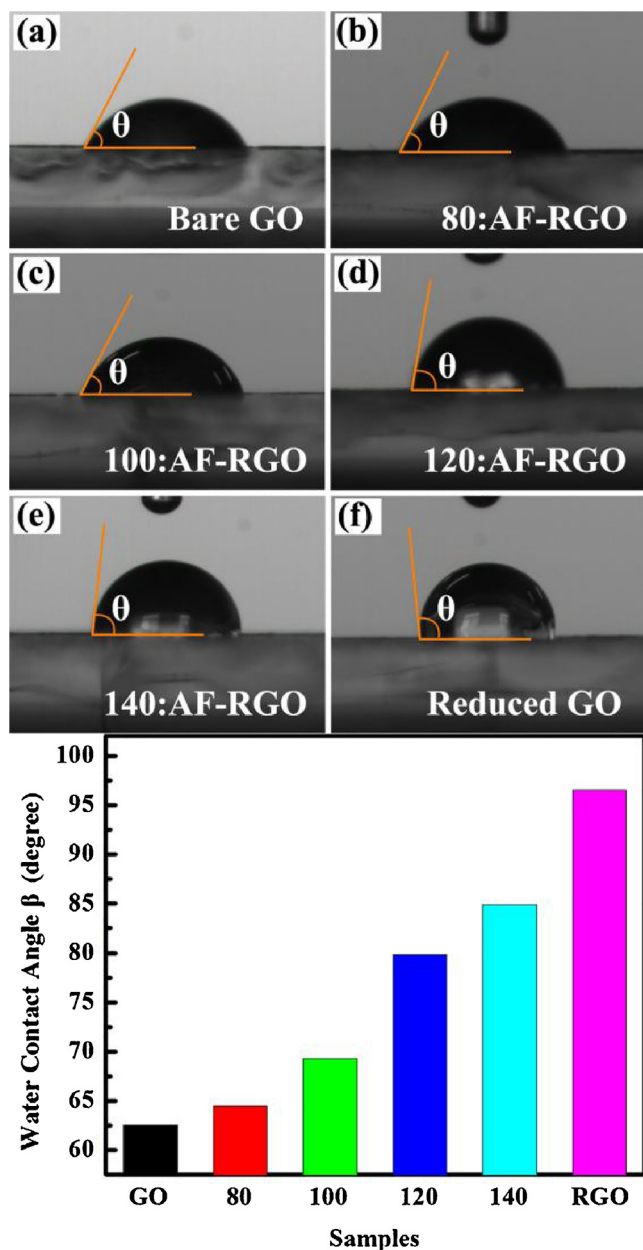
Fig. 2. (a–e) The photographs of water contact angle of bare GO, T:AF–RGO (T = 80, 100, 120 and 140 °C) and N_2H_4 solution reduced GO (RGO). (g) The histogram of samples corresponds to water contact angle.

the current curve is asymmetric in the whole range of the scanning voltage and shows a Schottky barrier characteristics [45,46]. The electrons with high kinetic energy can go across the Schottky barrier at the higher scanning voltage, but the electrons are confined at lower scanning voltage. The current curves of 80:AF–RGO and 100:AF–RGO show similar change tendency and properties owing to residue abundant of oxygen–containing groups. For the 120:AF–RGO and 140:AF–RGO, the current curves are relatively smooth and symmetrical, indicating the samples possess Ohmic behaviors and have a smaller resistance [46].

During solvothermal reaction of GO, the hydroxyl (0.30 eV) and epoxy (0.83 eV) groups can easily formed over the GO basal plane [35,47]. Thus, when sample was heated at 80 and 100 °C for 12 h, the isolated sp^3 fragments could effectively interact with the larger sp^3 domains, leading to phase separation of the sp^2 and sp^3 domains and forming larger sp^2 graphitic/planar domains, which enhanced the

conductivity of samples compared with bare GO [47]. When raw material was heated at higher temperature such as 120 °C, the phase separation took place very fast and led to the dehydration and decarbonation of hydroxyl and epoxy groups, which made the electrical properties of samples greatly improved. When the reaction temperature was up to 140 °C, the two reactions took place completely in the sp^3 domains. Thus, the 140:AF–RGO sample exhibited high conductivity. At the same time, the reduction of oxygen–containing groups led to the formation of the nitrogen functional groups.

The electronic properties of samples are further evaluated using 4–probe Hall measurement method at room temperature and the results are as shown in Table 1. The electrical data of bare GO and 80:AF–RGO were not measured due to their poor conductive performances. Interestingly, the major carrier in 100:AF–RGO, 120:AF–RGO and 140:AF–RGO samples is hole, and samples exhibit p–type conductive property. Especially, the 140:AF–RGO gives the ultrahigh carrier concentration of 2.219×10^{19} cm^{-3} and mobility of 8.358×10^{-1} cm^2/vs, partially due to the removing of most oxygen–containing functional groups on the surface of graphene. It is found that the conductivity of T:AF–RGO improves gradually with the increase of solvothermal treatment temperature.

Fig. 7a to t show the TEM images and Pt particle distribution of the GO/Pt and T:AF–RGO/Pt catalysts, respectively. The comparatively large Pt particles on GO indicates Pt NPs aggregation, however, Fig. 7d, g, j and m show that the dispersed Pt particles on T:AF–RGO/Pt catalyst is quite uniform. In addition, the dispersion of Pt particle is getting better when the solvothermal temperature increase. The HRTEM images in Fig. 7b, e, h, k and n show clear Pt lattice fringes of two orientations, and the inter–planar distances are 0.19 and 0.23 nm, which is consistent with the (100) and (111) Pt crystal planes [32]. Fig. 7c, f, i, l and o are the histograms of particle size, the average particle sizes are approximately 4.13, 4.08, 3.89, 3.72 and 3.10 nm by measurement for the diameters of 100 randomly selected particles. Moreover, the mapping of element clearly shows that the distribution of C, O, N and Pt are relatively homogeneous as shown in Fig. 7p–t.

3.3. Catalytic activity test

It is well known that the solubility of O_2 in water is much higher than that of H_2, which makes fish alive in the water. But high concentration of oxygen in the water leads to the fast hydrogen and oxygen recombination over the catalyst. To achieve effective hydrogen evolution via photocatalytic overall water splitting, the H_2 and O_2 recombination reaction over the photocatalyst dispersion must be considered and must be inhibited to some extent. We studied the hydrogen and oxygen recombination reaction over Pt, GO/Pt and T:AF–RGO/Pt catalysts before testing their activities for hydrogen evolution. The hydrogen and oxygen recombination rate was monitored by measuring the concentration of hydrogen in the catalyst–water dispersion in a sealed reactor. Fig. 8a presented the rates of recombination reaction over catalyst samples. The concentration of hydrogen decreases over all catalysts with the time under dark, indicating that the hydrogen and oxygen recombination reaction takes place in all the catalysts, however, different catalysts give different recombination curves. For example, the recombination over Pt nano–particle itself takes place very fast, however, the recombination undergoes much slower over deposited Pt co–catalyst, especially over the amide group modified graphene catalyst. These results demonstrated that amide groups on graphene can significantly affect the hydrogen and oxygen recombination reaction. The corresponding H_2 recombination rates in different catalysts are calculated [26], and the results are shown in the inset Fig. 8a.

The oxygen partial pressure in the reactor affects the recombination reaction significantly. As shown in Fig. 8b, the concentration of hydrogen in the reactor continuously decreased when the oxygen in atmosphere was bubbled by argon. That means that hydrogen can be activated and recombined with the dissolved oxygen in the water
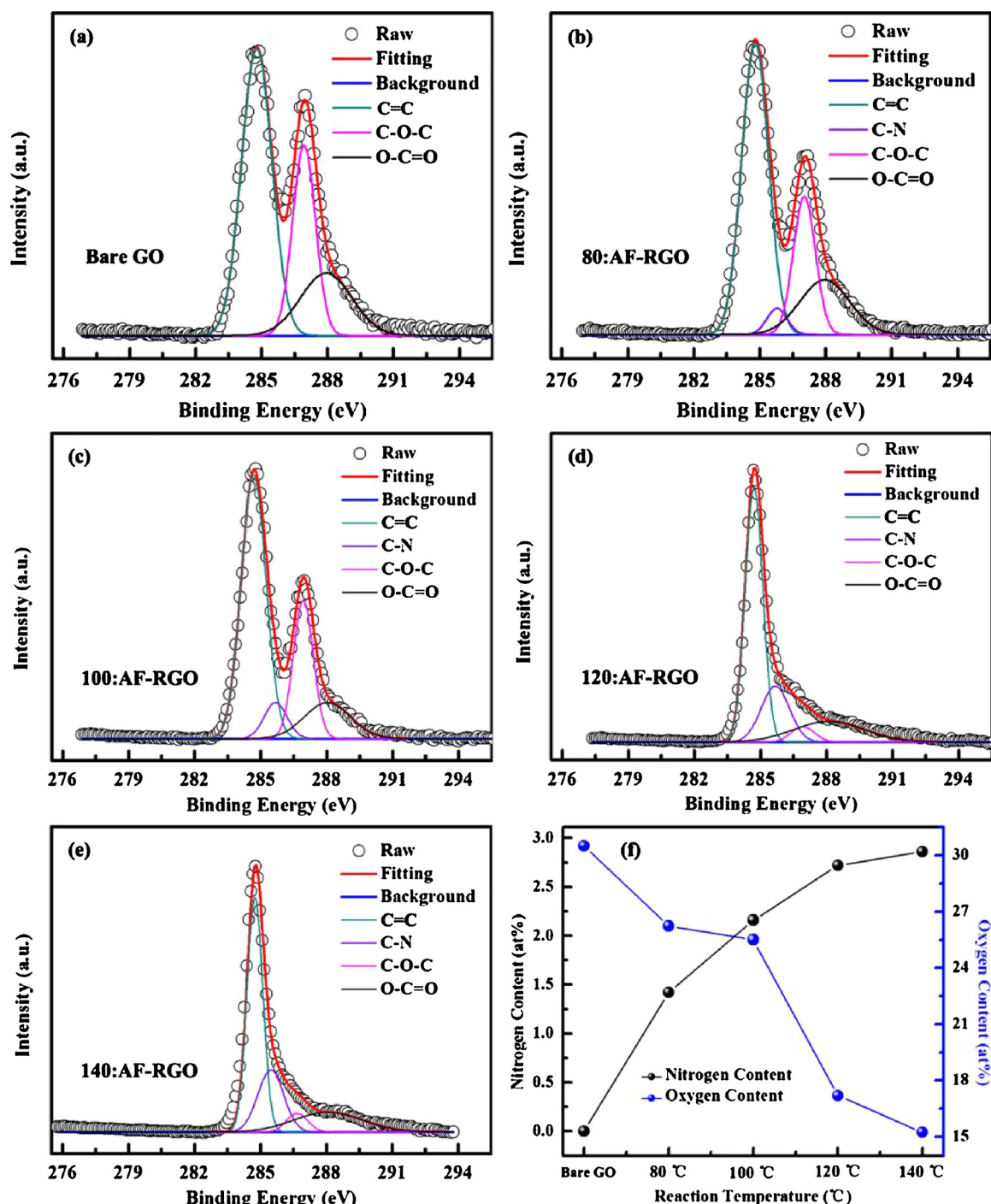
Fig. 3. XPS C1 s spectra of the bare GO (a) and T:AF–RGO obtained in DMF at different reaction temperatures of 80 (b), 100 (c), 120 (d) and 140 °C (e). (f) Corresponding variations of nitrogen and oxygen content with reduction temperature.

although the rate was lower than that when the oxygen is added in. As presented in Fig. S7, simultaneously adding hydrogen and oxygen can significantly enhance the rate of hydrogen and oxygen recombination over catalysts, implying that the recombination reaction is dependent on the oxygen partial pressure.

The time courses of photocatalytic hydrogen evolution over the catalysts are studied and results are shown in Fig. 9a. EY–sensitized Pt without GO after irradiation 2 h produces 202.4 μmol H_2 [48,49]. After loading Pt NPs on the surface of bare GO, 380.9 μmol hydrogen is obtained over the EY–sensitized GO/Pt photocatalyst in 2 h. The EY–-sensitized T:AF–RGO/Pt (T = 80, 100, 120 and 140 °C) photocatalyst give high hydrogen generation rate, 408.2, 604.1, 700.9 and

771.1 μmol of hydrogen are obtained under same irradiation conditions, respectively. Moreover, the hydrogen evolution over N_2H_4 solution reduced RGO/Pt nanoparticles is 572.5 μmol (see Fig. S8). Especially, the 140:AF–RGO/Pt present the highest hydrogen generation activity compared with other catalysts, which are 2.02, 1.89, 1.28 and 1.10 times higher than that of GO/Pt, 80:AF–RGO/Pt, 100:AF–RGO/Pt and 120:AF–RGO/Pt. 140:AF–RGO/Pt also exhibits a high stability and repeatability in the four cycles photocatalytic H_2 evolution, as shown in Fig. S9. In Table S1, the H_2 evolution rate of 140:AF–RGO/Pt is higher than those of most of graphene/Pt nanoparticles based catalyst. The enhancement of hydrogen evolution reflected the strong inhibition role of amide groups on hydrogen and oxygen recombination.
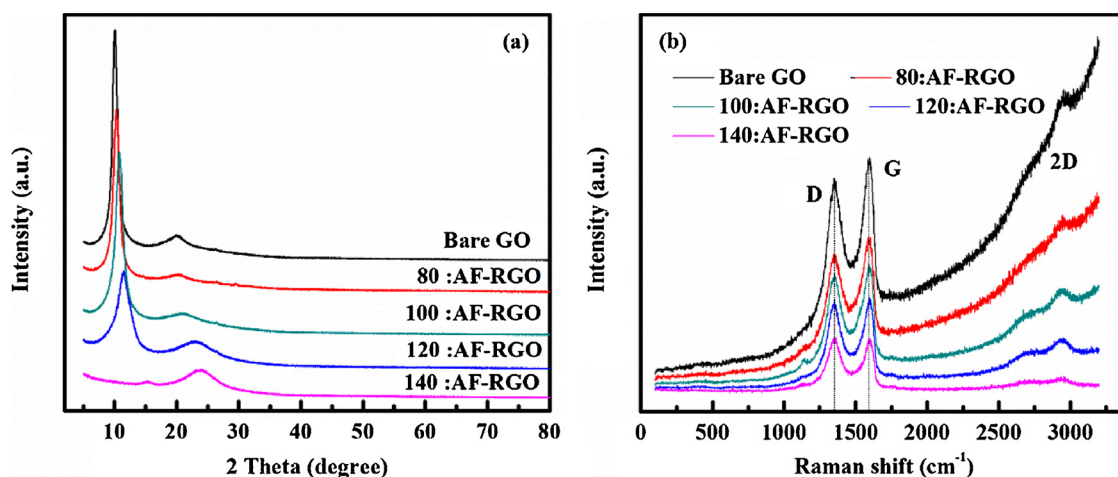
Fig. 4. (a) XRD patterns and (b) Raman spectra of the bare GO and T:AF–RGO obtained in DMF at different reaction temperatures of 80, 100, 120 and 140 °C, respectively.
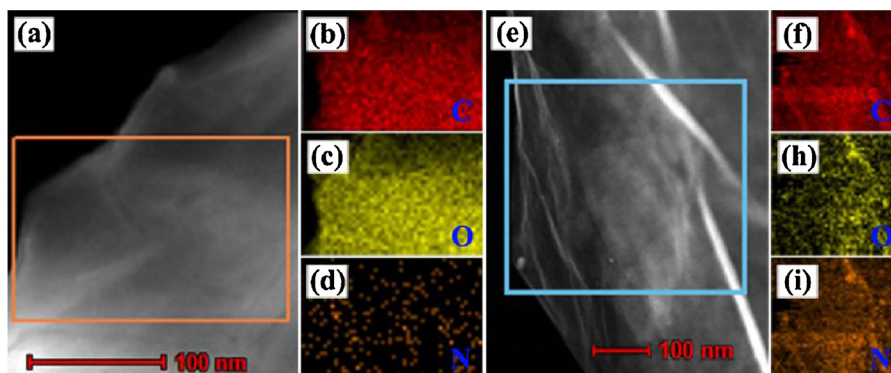

Fig. 5. (a–i) Representative HAADF–STEM and elemental mapping of the bare GO and 140:AF–RGO reveal that atoms are homogeneously distributed over the whole surface of samples.
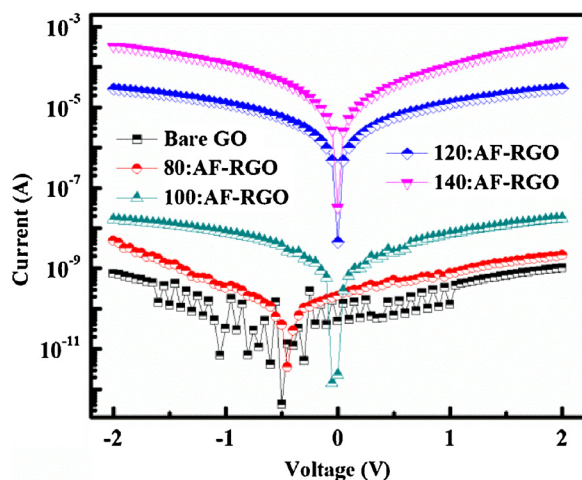

Fig. 6. I–V characteristics of bare GO and T:AF–RGO obtained in DMF at different reduction temperatures of 80, 100, 120 and 140 °C, respectively.

Table 1
Comparison of several electrical parameters extracted from Hall measurement of bare GO and T:AF–RGO (T = 80, 100, 120 and 140 °C). The carrier concentration, mobility and resistivity are denoted as Nb, μ and rho, respectively.

Samples	GO	80:AF–RGO	100:AF–RGO	120:AF–RGO	140:AF–RGO
Nb (cm^{-3})	–	–	3.769×10^9	5.209×10^{18}	2.219×10^{19}
μ (cm^2/vs)	–	–	3.351×10^{-2}	8.033×10^{-1}	8.358×10^{-1}
rho (Ω/cm)	–	–	4.943×10^6	1.492	3.366×10^{-1}

which corresponds to the strongest absorption wavelength of EY at 518 nm in Fig. S10. To optimize the reaction condition, the effect of pH on photocatalytic activity of 140:AF–RGO/Pt for hydrogen generation is presented in Fig. S11. The highest activity of hydrogen evolution is achieved to 862.5 μmol at pH = 9. The H$_2$ evolution activity gradually decreases with the acidity increase, due to the protonation of TEOA in acidic solution, which can impact the electron–donating properties of TEOA and the absorption performance of EY in the visible light region [52,53]. Addition of alkaline results in the decrease of proton concentration and the decrease of hydrogen evolution over 140:AF–RGO/ Pt, for example, only 477.8 μmol of H$_2$ is detected in 2 h at pH = 11. More results were presented in Figs. S12 and S13.

In order to prove the hydrogen is generated from photocatalytic water splitting, the isotopic tracer experiment was carried out and gas products were analyzed by Gas Chromatography Mass Spectrometer (GC–MS). As shown in Fig. 10a, D$_2$ was produced by D$_2$O splitting over 140:AF–RGO/Pt photocatalyst under visible light irradiation for 4 h. Trace amount of H$_2$ was formed due to the proton exchange [54–57].
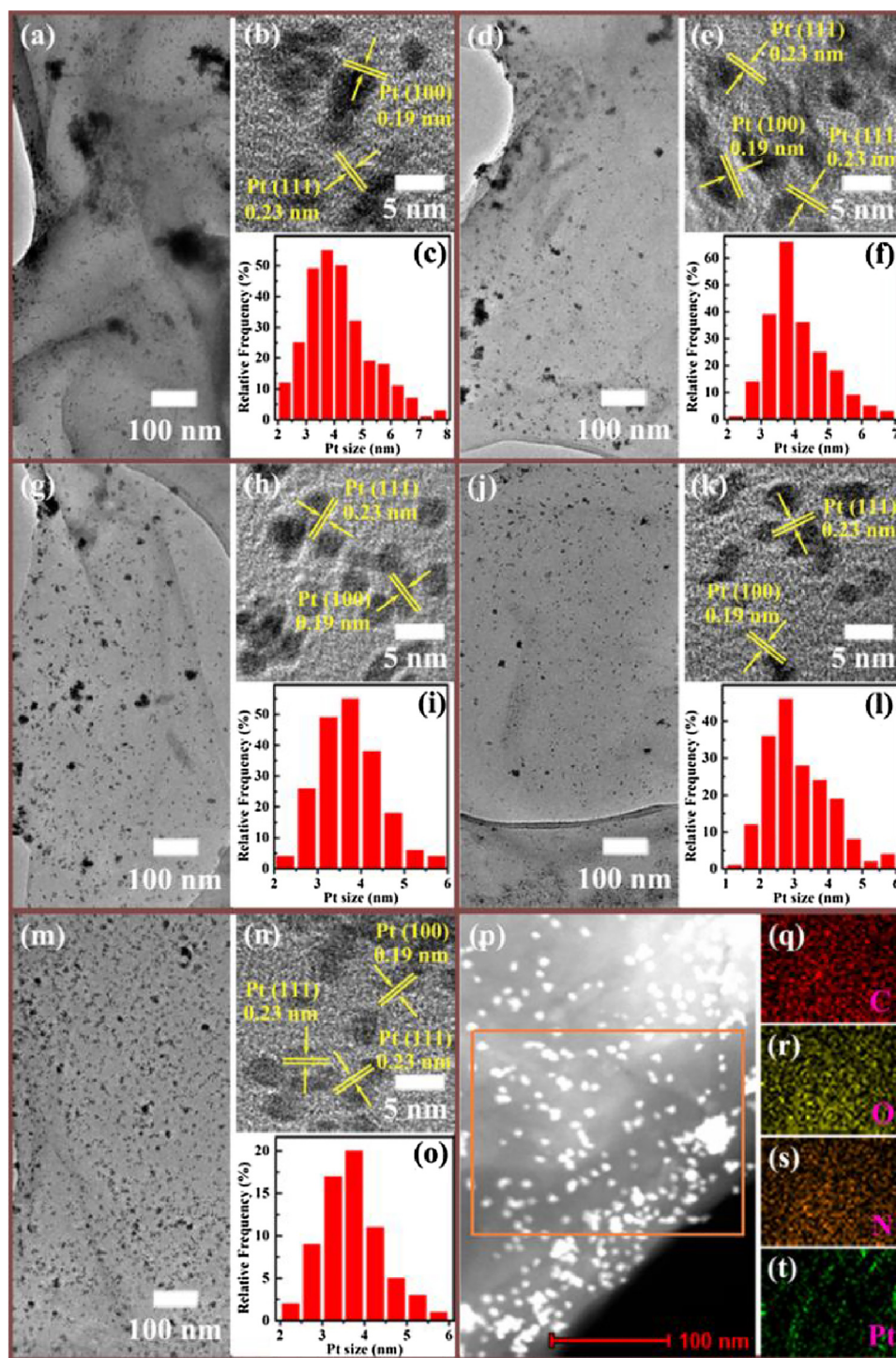
In Fig. 9b, the AQEs of catalysts for hydrogen evolution were measured under illumination of 430–600 nm light using various band pass filters (λ = 430, 460, 490, 520 and 550 nm). The highest AQE reaches 36.4% at 430 nm for the 140:AF–RGO/Pt system compared with GO/Pt (17.9%), 80:AF–RGO/Pt (16.9%), 100:AF–RGO/Pt (25.4%) and 120:AF–RGO/Pt (31.2%) catalysts. With the incident light wavelength increased, the AQEs value decrease gradually owing to the lower photon energy [50,51]. The second highest AQEs appears at 520 nm,

Fig. 7. (a), (d), (g), (j) and (m) show the low magnification TEM of the bare GO/Pt, 80:AF–RGO/Pt, 100:AF–RGO/Pt, 120:AF–RGO/Pt and 140:AF–RGO/Pt; (b), (e), (h), (k) and (n) represent corresponding HRTEM images; (c), (f), (i), (l) and (o) indicate corresponding distributing maps of Pt particle size; (p)–(t) represent corresponding HAADF–STEM images and elemental mapping images of the 140:AF–RGO/Pt.

The over–potential of hydrogen generation over different catalyst was also studied by electrochemical method. Fig. 10b displays the current curves under different bias voltage. The 140:AF–RGO/Pt deposited electrode gave lower over–potential compared with other samples. The transient photocurrent responses of the samples over several on–off cycles of visible light irradiation are shown in Fig. S14. Good reproducibility and stability were observed over 140:AF–RGO/Pt catalyst.

The photoluminescence and time–resolved photoluminescence (TRPL) are carried out to gain insight into the separation and re-combination of photogenerated charge carriers. As shown in Fig. 10c, the EY solution shows an intensive emission peak centered at 534 nm, which is caused by its strong recombination of excited charge pairs by exciting visible light [32,49]. When GO/Pt and T:AF–RGO/Pt are used, the peak intensity of EY emission is significantly decreased. The quenching efficiency of 140:AF–RGO/Pt (67.9%) is remarkably higher than others due to the rapid transfer of photogenerated charges from EY to sensitized graphene matrix and Pt NPs. In Fig. 10d, the TRPL of EY in
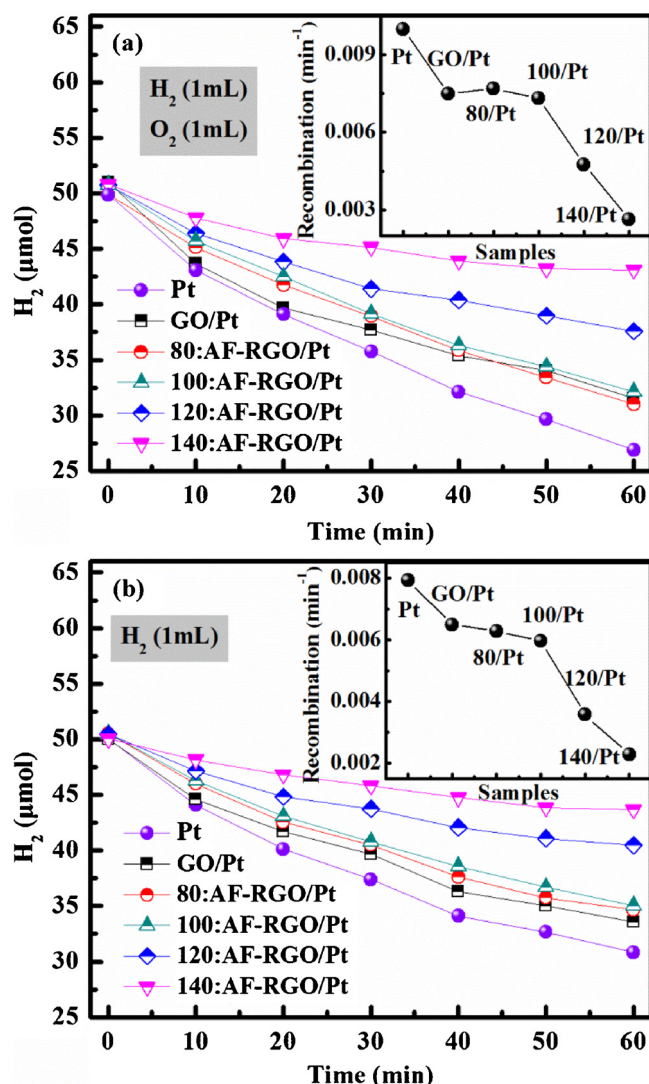
Fig. 8. (a) The time courses of the H_2 and O_2 recombination reaction over Pt, GO/Pt and T:AF–RGO/Pt catalysts in a sealed Pyrex flask by injecting 1 mL H_2 and 1 mL O_2 into the reactor at room temperature. (b) The hydrogen and oxygen recombination reaction of different catalysts measured with 1 mL H_2. The corresponding H_2 recombination rates for different catalysts.
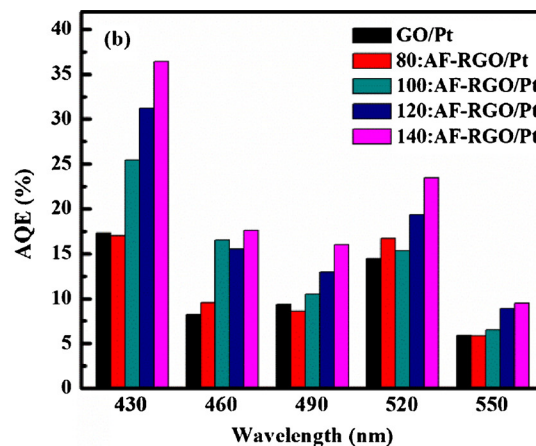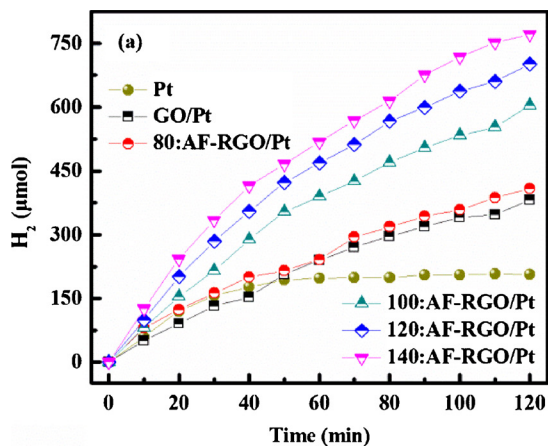
the presence of GO/Pt and T:AF-RGO/Pt are presented. The lifetime of 140:AF–RGO/Pt is longer than other samples. The fluorescence lifetime τ, which is determined according to reported method [58], are obtained by fitting the decay profiles with one and two exponential terms, these data of lifetimes are given in Table S2. The fluorescence lifetime of EY is 0.92 ns, which increases to 1.21, 1.24, 1.28, 1.42 and 1.50 ns the presence of GO/Pt, 80:AF–RGO/Pt, 100:AF–RGO/Pt, 120:AF–RGO/Pt and 140:AF–RGO/Pt respectively. These results indicate that the lifetime of the singlet excited EY^{1*} could be prolonged in T:AF–RGO/Pt/EY systems. The long lifetime of EY^{1*} can greatly facilitate the production of lowest–lying triplet excited state (EY^{3*}) via the intersystem crossing (ISC) [1,49], which is beneficial for the generation of $EY^{·-}$.

The photocatalytic hydrogen evolution process over 140:AF–RGO/Pt catalyst can be depicted in Scheme 2. It is known that hydrogen bond interaction is a critical factor to achieve long–range donor–acceptor electronic coupling [11,59]. Due to hydrogen bond between EY and 140:AF–RGO, the electron transfer can achieve between photoexcited EY and 140:AF–RGO. The adsorbed EY molecule on graphene is first excited by visible light, formed the singlet excited–state (EY^{1*}) via electron transition from its HOMO to LUMO under visible–light irradiation (reaction (4)). By the ISC, the long–lived EY^{1*} can convert into the lowest–lying triplet excited state (EY^{3*}) as shown in reaction (5). TEOA can effectively quench EY^{3*} to produce reductive radical $EY^{·-}$ and oxidative donor $TEOA^+$ (reaction (6)) [60]. Since the formed $EY^{·-}$ radical is very stable [61,62], $EY^{·-}$ on 140:AF–RGO surface can inject the electron into p–type 140:AF–RGO (reaction (7)) [39,40]. Due to superior conductivity and p–type properties of 140:AF–RGO, the injected electrons can be effectively transferred along the surface of 140:AF–RGO to hydrogen evolution sites, such as Pt (reaction (8)) [32,62], then solar light driven reduction of H^+ to form H_2 is achieved according to reaction (9).

$$EY \xrightarrow{h\nu} EY^{1*} \ (\nu \geq 420\,nm) \tag{4}$$

$$EY^{1*} \xrightarrow{ISC} EY^{3*} \tag{5}$$

$$EY^{3*} + TEOA \ (\rightarrow) \ EY^{·-} + TEOA^+ \tag{6}$$

$$EY^{·-} + T:AF\text{-}RGO \ (\rightarrow) \ T:AF\text{-}RGO^- + EY \tag{7}$$

$$PtCl_6^{2-} + 4T:AF\text{-}RGO \ (\rightarrow) \ Pt + 4T:AF\text{-}RGO^- + 6Cl_6^- \tag{8}$$

$$2H_2O + 2T:AF\text{-}RGO^- \xrightarrow{Pt} 2T:AF\text{-}RGO + 2OH^- + H_2\uparrow \tag{9}$$

As discussed above, the formed hydrogen may react with dissolved oxygen in water to form water again. Therefore, it is necessary to consider the oxygen combination performance over the amide
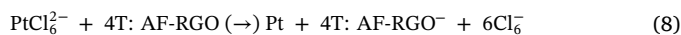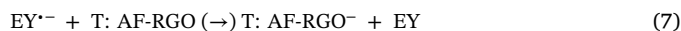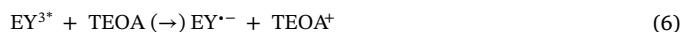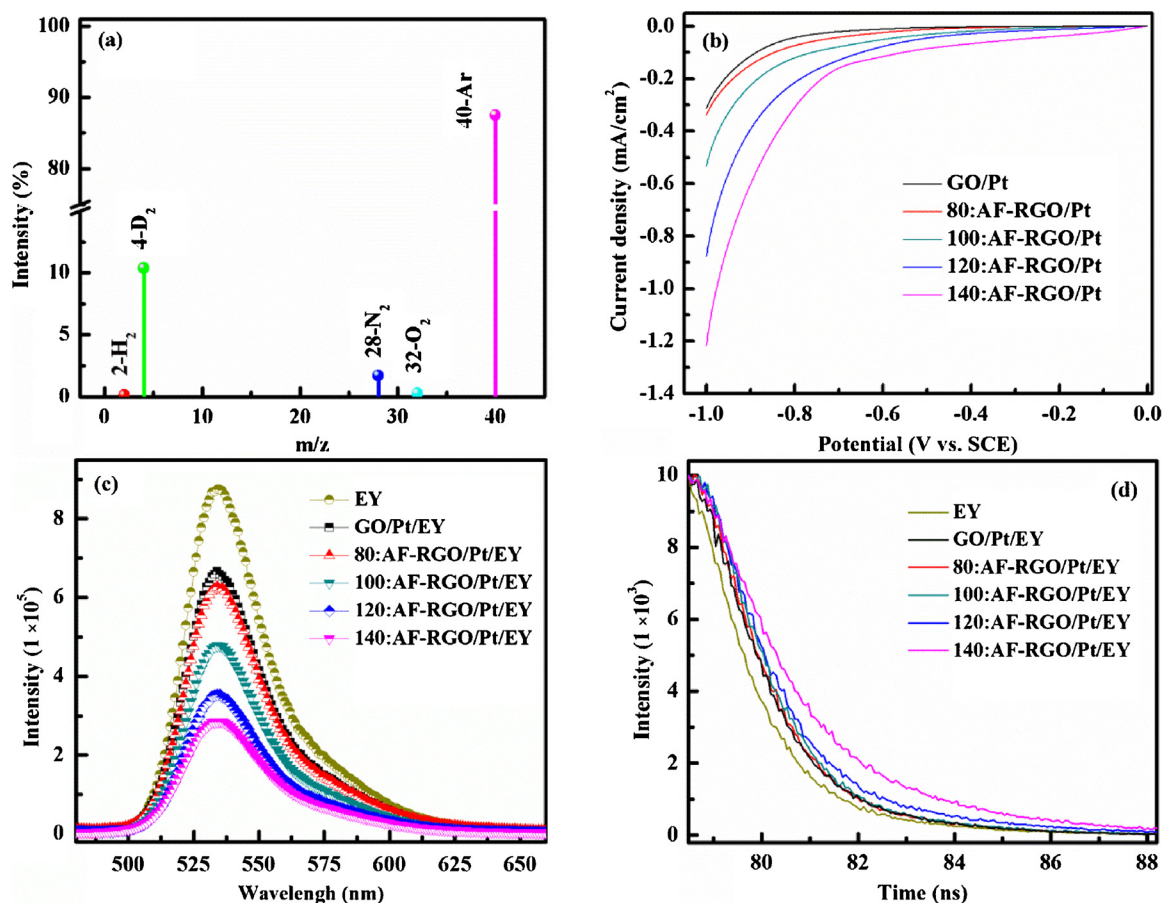

Fig. 9. (a) The amount of H_2 evolution by EY photosensitized systems catalyzed Pt loaded on the bare GO and T:AF–RGO in 100 mL 10% (v/v) TEOA aqueous solution (pH = 7) under visible light irradiation (λ ≥ 420 nm). (b) AQE of GO/Pt, 80:AF–RGO/Pt, 100:AF–RGO/Pt, 120:AF–RGO/Pt and 140:AF–RGO/Pt EY–sensitized system under different wavelengths of visible light irradiation.

Fig. 10. (a) GC–MS spectrum obtained after injecting 0.5 mL samples of the gas phase species produced by D_2O splitting over 140:AF–RGO/Pt photocatalyst in a sealed Pyrex flask under visible light irradiation for 2 h. The m/z signal at 2, 4, 28, 32 and 40 correspond to the H_2, D_2, N_2, O_2 and Ar gas. (b) Linear sweep voltammetry curves of EY photo–sensitized GO/Pt and T:AF–RGO/Pt coated on ITO glass. (c) Photoluminescence and (d) time–resolved photoluminescence (TRPL) spectra of EY, GO/Pt and T:AF–RGO/Pt systems at an excitation wavelength of 464 nm.
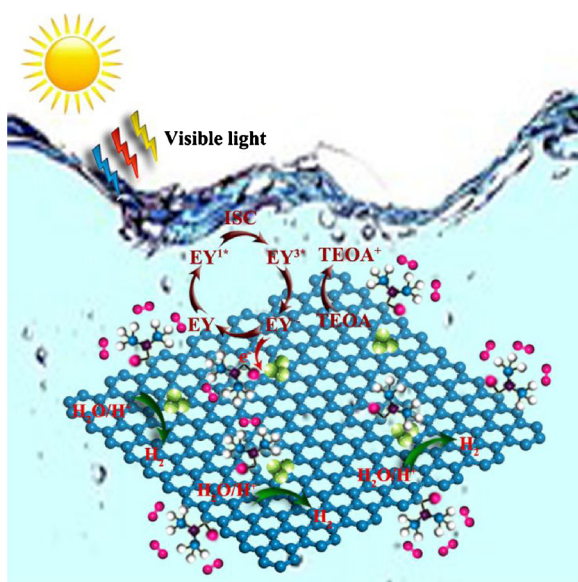
Scheme 2. The proposed photocatalytic mechanism for hydrogen evolution over the AF–RGO/Pt in EY system under visible light irradiation.

functional group modified graphene. Remember the amide groups can remarkably inhibit the rate of hydrogen and oxygen recombination reaction. To reveal the mechanism and interaction between the O_2 molecules and amide groups, we use the first–principle method to study

the interaction between oxygen and amide group [63]. Finite cluster model is used for calculation by the density functional theory with Perdew–Burke–Ernzerhof (PBE) functional. The double–zeta split basis sets with polarization functions 6–31G (d,p) are employed as well. The computations are performed using Gaussian 09 program.

O_2 adsorption on amide group graphene can be simplified as a cluster with 24 carbon atoms, both flawless and amide–functionalized cluster model expression of the graphene and AF–RGO, respectively, as shown in Fig. 11. The dangling bonds of the C atoms at the boundary are terminated with H atoms. The optimized and representative cluster models of graphene and AF–RGO with one O_2 molecule adsorbed over the surface of graphene (Fig. 12a and b) and amide group modified AF–RGO catalyst (Fig. 12c, d and e) are simulated where the dangling bonds of the C also are terminated with H. The adsorption energy (E_{ad}) are calculated by

$$E_{ad} = E_{mole + slab} - E_{slab} - E_{mole} \qquad (10)$$

where $E_{mole + slab}$, E_{slab} and E_{mole} are the total energies of the complex systems of surfaces and O_2 molecules, the energy of isolated surfaces, and the energy of free O_2 molecules, respectively [63,64]. The different adsorption manners are examined and E_{ad} of stable configurations are summarized in Fig. 12. For the O_2 molecules adsorptions on graphene, the most favorable site trends to the fringe and the E_{ad} is $- 4.40$ kJ/mol. When the effect of amide functional groups is considered, the adsorption sites are divided into three categories by distance from the groups to O_2. It is worth noting that the introduction of amide functional groups makes the O_2 adsorption energy and strength on the AF–RGO obviously increase compared with the adsorption on graphene. The
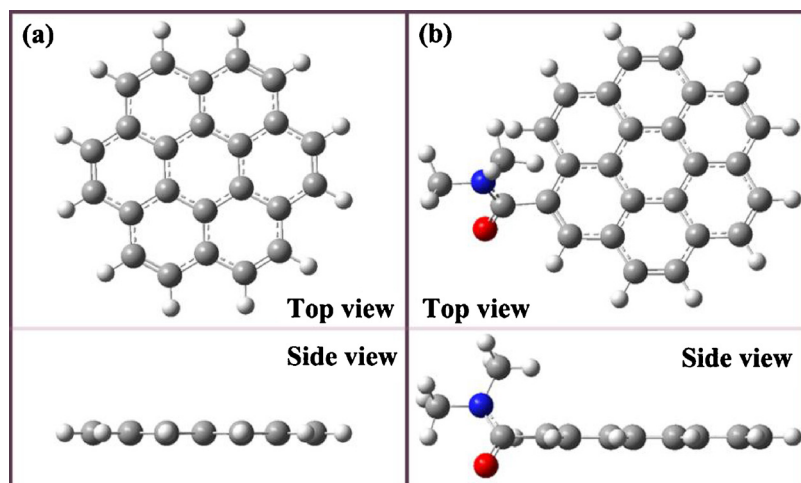
Fig. 11. (a) and (b) Representative top and side views of a cluster model of graphene and AF–RGO, respectively. All of the edge C atoms are saturated with dangling H. The gray, red, blue and white balls are carbon, oxygen, nitrogen and hydrogen atoms in this figure and figures below. (For interpretation of the references to colour in this figure legend, the reader is referred to the web version of this article).

relatively most stable adsorption shown in Fig. 12d, and its E_{ad} can reach to –21.71 kJ/mol due to the effect of amide group, which lead to easier O_2 molecule absorbed by the amide functional groups of AF–RGO.

In order to explain the calculation results, the partial density of states (PDOS) of N atoms of amide functional groups and O atom of O_2 molecule are plotted and shown in Fig. 13a. The density is calculated using the Multiwfn program and the energy levels are represented by Gaussian distribution with a half width of 0.2 eV. There is a strong overlap between the N 2p and O 2p in the range −14.97 to −11.25 eV. This indicates the strong interaction between O_2 molecules with amide

functional groups. Fig. 13b displays the electron density difference of the AF–RGO with one adsorbed O_2 molecule with a 0.0024 eÅ^{-3} iso-surface value. The isosurface is obtained by subtracting the electron density of the isolated O_2 molecules and AF–RGO from that of the O_2 adsorbed AF–RGO. The violet color represents electron accumulation and the cyan color represents electron depletion. We find that there is an increase of electron density in the region of O_2 and an electron density on the amide functional groups of AF–RGO, but there is no completely electrostatic interaction between them. This implies that O_2 molecules are prefer to adsorb on the AF–RGO, corresponding to the increase of adsorption energy due to the orbital hybridization of the O
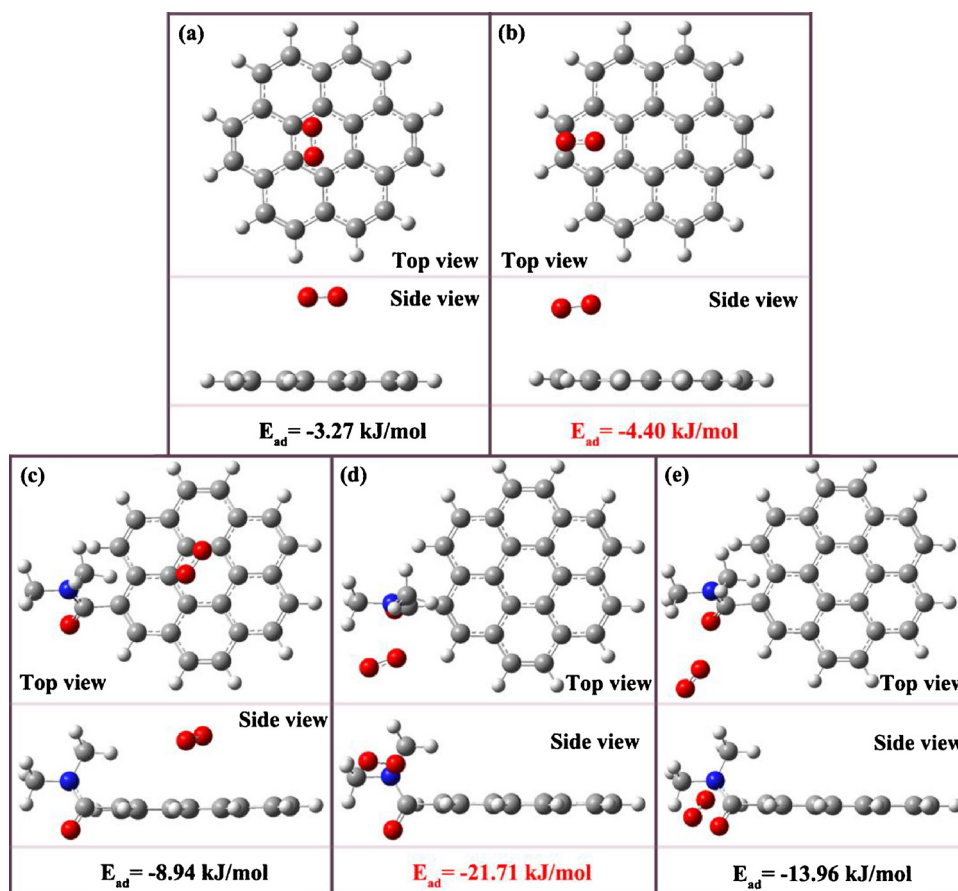

Fig. 12. (a) and (b) Two optimized adsorption configurations for a O_2 molecule absorbed on the surface of graphene. (c), (d) and (e) Three optimized adsorption configurations on amide functional groups of AF–RGO, respectively. E_{ad} is adsorption energy in the all of configurations.
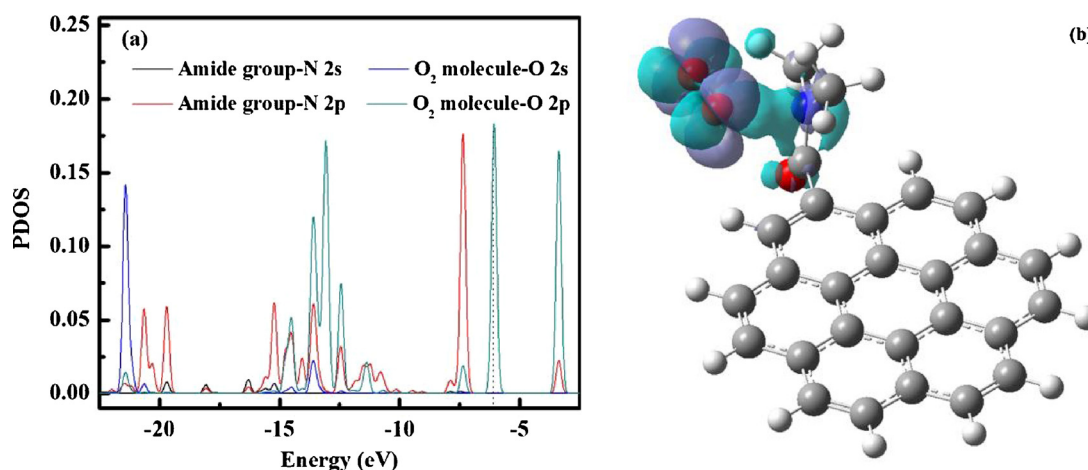
Fig. 13. (a) Partial density of states of N atoms of amide functional groups and O_2 molecule in the systems of adsorption on AF–RGO. The dashed lines are HOMO levels. (b) the electron density difference of the AF–RGO with one adsorbed O_2 molecule with a 0.0024 e Å^{-3} isosurface value. The violet color represents electron accumulation and the cyan color represents electron depletion.

2p and N 2p orbitals [64]. The strong dependence between the O_2 adsorption and the amide functional groups in AF–RGO determine the electronic structure of catalyst and impact its ability to inhibit reverse recombination of hydrogen and oxygen.

4. Conclusions

In this work, AF–RGO is prepared via a liquid phase solvothermal treatment using DMF as the dispersing and reducing agent. By controlling and adjusting the reaction temperature from 80 to 140 °C, incorporating amide groups onto graphene has been achieved. The hydrophobic property was enhanced in some extend by this treatment due to replacement oxygen–containing functional group by amide group on GO. Amide group modification also improves the electrical properties of catalyst, such as conductivity, carrier concentration and mobility. In addition, the formed amide groups can act as the oxygen adsorbent, with the adsorption energy E_{ad} up to -21.71 kJ/mol due to forming orbital hybridization by N 2p in amide group with O 2p in O_2 molecule, leading to decrease of migration of dissolved O_2 molecules and restraining H_2 and O_2 recombination. These properties make catalyst exhibit excellent photocatalytic activity for the H_2 generation from water. The as–prepared AF–RGO/Pt nanohybrid catalyst shows the highest H_2 generation activity compared with other catalysts. The quantum efficiency of 140:AF–RGO/Pt can achieve 36.4% at 430 nm. The findings in this work will remarkably improve the performances of graphene–based sensitized catalyst for PHE.

Acknowledgement

Appendix A. Supplementary data

Supplementary material related to this article can be found, in the online version, at doi:https://doi.org/10.1016/j.apcatb.2018.03.070.

References

[1] C. Kong, S.X. Min, G.X. Lu, ACS Catal. 4 (2014) 2763–2769.
[2] Z.Y. MA, X.B. Li, L.J. Deng, G. Fan, J. Mol. Catal. (China) 30 (2016) 575–582.
[3] K. Maeda, G. Sahara, M. Eguchi, O. Ishitani, ACS Catal. 5 (2015) 1700–1707.
[4] G.X. Lu, B. Tian, J. Mol. Catal. (China) 31 (2017) 101–104.
[5] B. Tian, W.L. Zhen, H.B. Gao, X.Q. Zhang, Z. Li, G.X. Lu, Appl. Catal. B 203 (2017) 789–797.
[6] Y.Z. Xie, X. Wang, S.Q. Liu, L.C. Guo, L. Zhao, J. Mol. Catal. (China) 30 (2016) 372–382.
[7] Z. Li, Q.S. Wang, C. Kong, Y.Q. Wu, Y.X. Li, G.X. Lu, J. Phys. Chem. C 119 (2015) 13561–13568.
[8] G.X. Lu, W.L. Zhen, J. Mol. Catal. (China) 31 (2017) 299–304.
[9] X. Zhang, T. Peng, L. Yu, R. Li, Q. Li, Z. Li, ACS Catal. 5 (2015) 504–510.
[10] Lu Q, C.L. Li, F. Wang, Q.J. Ren, Z. Ren, J. Mol. Catal. (China) 30 (2016) 557–565.
[11] W.Y. Zhang, Y.X. Li, S.Q. Peng, ACS Appl. Mater. Interfaces 8 (2016) 15187–15195.
[12] Z.X. Huang, Y.F. Li, Y.X. Li, S.Q. Peng, J. Mol. Catal. (China) 31 (2017) 181–187.
[13] Y.G. Lei, C. Yang, J.H. Hou, F. Wang, S.X. Min, X.H. Ma, Z.L. Jin, J. Xu, G.X. Lu, K.W. Huang, Appl. Catal. B 216 (2017) 59–69.
[14] G.X. Lu, W.Y. Zhang, J. Mol. Catal. (China) 31 (2017) 401–410.
[15] X.Q. Zhang, G.X. Lu, Carbon 108 (2016) 215–224.
[16] J. Ni, X.F. Luo, Y. Zhan, J.X. Lin, J. Mol. Catal. (China) 30 (2016) 282–296.
[17] Q.L. Zhou, L. Li, C.L. Yang, Y.Z. Jiao, X.Y. Zhang, J. Mol. Catal. (China) 31 (2017) 236–246.
[18] Y.H. Li, C. Peng, S. Yang, H.F. Wang, H.G. Yang, J. Catal. 330 (2015) 120–128.
[19] A. Bruix, J. Rodriguez, P. Ramírez, S. Senanayake, J. Evans, J. Park, D. Stacchiola, P. Liu, J. Hrbek, F. Illas, J. Am. Chem. Soc. 134 (2012) 8968–8974.
[20] H. Zhao, Y.M. Dong, P.P. Jiang, H.Y. Miao, G.L. Wang, J.J. Zhang, J. Mater. Chem. A 3 (2015) 7375–7381.
[21] L.G. Kong, Y.M. Dong, P.P. Jiang, G.L. Wang, H.Z. Zhang, N. Zhao, J. Mater. Chem. A 4 (2016) 9998–10007.
[22] Y.M. Dong, L.G. Kong, P.P. Jiang, G.L. Wang, N. Zhao, H.Z. Zhang, B. Tang, ACS Sustain. Chem. Eng. 5 (2017) 6845–6853.
[23] Y.M. Dong, L.G. Kong, G.L. Wang, P.P. Jiang, N. Zhao, H.Z. Zhang, Appl. Catal. B 211 (2017) 245–251.
[24] H. Zhao, H.Z. Zhang, G.W. Cui, Y.M. Dong, G.L. Wang, P.P. Jiang, X.M. Wu, N. Zhao, Appl. Catal. B 225 (2018) 284–290.
[25] M. Wang, Z. Li, Y.Q. Wu, J.T. Ma, G.X. Lu, J. Catal. 353 (2017) 162–170.
[26] Z. Li, B. Tian, W.L. Zhen, Y.Q. Wu, G.X. Lu, Appl. Catal. B 203 (2017) 408–415.
[27] E. Lalik, R. Kosydar, R. Tokarz–Sobieraj, M. Witko, T. Szumełda, M. Kołodziej, W. Rojek, T. Machej, E. Bielańska, A. Drelinkiewicz, Appl. Catal. A 501 (2015) 27–40.
[28] G. Sang, X. Lai, W. Qian, W. Cao, C. Sheng, Y. Su, X. Ye, Energy Procedia 29 (2012) 552–558.
[29] Y.H. Li, J. Xing, Z.J. Chen, Z. Li, F. Tian, L.R. Zheng, H.F. Wang, P. Hu, H.J. Zhao, H.G. Yang, Nat. Commun. 4 (2013) 2500.
[30] X. Zhu, B. Cheng, J. Yu, W. Ho, Appl. Surf. Sci. 364 (2016) 808–814.
[31] H.W. Kang, S.B. Park, J.G. Kim, I.T. Kim, Int. J. Hydrogen Energy 39 (2014) 5537–5545.
[32] X.Q. Zhang, B. Tian, W.L. Zhen, Z. Li, Y.Q. Wu, G.X. Lu, J. Catal. 354 (2017) 258–269.
[33] S. Chen, J.J. Duan, J.R. Ran, M. Jaroniec, S.Z. Qiao, Energy Environ. Sci. 6 (2013) 3693–3699.
[34] S.Y. Li, Y. Li, J. Wang, Y.G. Nan, B.H. Ma, Z.L. Liu, J.X. Gu, Chem. Eng. J. 290 (2016) 82–90.
[35] D. Zhou, Q.Y. Cheng, B.H. Han, Carbon 49 (2011) 3920–3927.
[36] P. Barpanda, G. Fanchini, G.G. Amatucci, Electrochim. Acta 52 (2007) 7136–7147.
[37] Q. Tang, Z. Zhou, Z.F. Chen, Nanoscale 5 (2013) 4541–4583.
[38] R. Sitko, E. Turek, B. Zawisza, E. Malicka, E. Talik, J. Heimann, A. Gagor, B. Feist, R. Wrzalik, Dalton Trans. 42 (2013) 5682–5689.
[39] A. Gupta, G. Chena, P. Joshi, S. Tadigadapa, P.C. Eklund, Nano Lett. 6 (2006) 2667–2673.
[40] H. Wang, C. Zhang, Z. Liu, L. Wang, P. Han, H. Xu, K.J. Zhang, S.M. Dong, J.H. Yao, G.L. Cui, J. Mater. Chem. 21 (2011) 5430–5434.
[41] J.J. Teo, Y. Chang, H.C. Zeng, Langmuir 22 (2006) 7369–7377.
[42] Y. Chang, J.J. Teo, H.C. Zeng, Langmuir 21 (2005) 1074–1079.
[43] Y. Matsuo, T. Niwa, Y. Sugie, Carbon 37 (1999) 897–901.

[44] Y.Y. Liang, D.Q. Wu, X.L. Feng, K. Müllen, Adv. Mater. 21 (2009) 1679–1683.
[45] X.Q. Zhang, C.W. Wang, J.B. Chen, W.D. Zhu, A.Z. Liao, Y. Li, J. Wang, L. Ma, ACS Appl. Mater. Interfaces 6 (2014) 20625–20633.
[46] X.Q. Zhang, J.B. Chen, C.W. Wang, A.Z. Liao, X.F. Su, Nanotechnology 26 (2015) 175705.
[47] S. Park, J. An, I. Jung, R.D. Piner, S.J. An, X.S. Li, A. Velamakanni, R.S. Ruoff, Nano Lett. 9 (2009) 1593–1597.
[48] W.Y. Zhang, C. Kong, G.X. Lu, Chem. Commun. 51 (2015) 10158–10161.
[49] W.Y. Zhang, W. Gao, X.Q. Zhang, Z. Li, G.X. Lu, Appl. Surf. Sci. 434 (2018) 643–668.
[50] X.F. Ning, J. Li, B.J. Yang, W.L. Zhen, Z. Li, B. Tian, G.X. Lu, Appl. Catal. B 212 (2017) 129–139.
[51] W.Y. Zhang, C. Kong, W. Gao, G.X. Lu, Chem. Commun. 52 (2016) 3038–3041.
[52] Y. Numata, S.P. Singh, A. Islam, M. Iwamura, A. Imai, K. Nozaki, L. Han, Adv. Funct. Mater. 23 (2013) 1817–1823.
[53] H.B. Gao, W.L. Zhen, J.T. Ma, G.X. Lu, Appl. Catal. B 206 (2017) 353–363.
[54] W.L. Zhen, J.T. Ma, G.X. Lu, Appl. Catal. B 190 (2016) 12–25.
[55] X.F. Ning, W.L. Zhen, Y.Q. Wu, G.X. Lu, Appl. Catal. B 226 (2018) 373–383.
[56] W.L. Zhen, H.B. Gao, B. Tian, J.T. Ma, G.X. Lu, ACS Appl. Mater. Interfaces 8 (2016) 10808–10819.
[57] Z. Li, B. Tian, W.L. Zhen, W.Y. Zhang, X.Q. Zhang, Y.Q. Wu, G.X. Lu, Appl. Catal. B 219 (2017) 501–510.
[58] G. Williams, P.V. Kamat, Langmuir 25 (2009) 13869–13873.
[59] P.J. De Rege, S.A. Williams, M.J. Therien, Science 269 (1995) 1409–1413.
[60] Z.J. Han, W.R. McNamara, M. Eum, P.L. Holland, R.A. Eisenberg, Angew. Chem. Int. Ed. 51 (2012) 1667–1670.
[61] V. Kasche, L. Lindqvist, Photochem. Photobiol. 4 (1965) 923–933.
[62] Y. Matsumoto, M. Koinuma, S. Ida, S. Hayami, T. Taniguchi, K. Hatakeyama, H. Tateishi, Y. Watanabe, S. Amano, J. Phys. Chem. C 115 (2011) 19280–19286.
[63] Z.M. Ao, F.M. Peeters, Phys. Rev. B 81 (2010) 205406.
[64] C. Ataca, E. Aktürk, S. Ciraci, Phys. Rev. B 79 (2009) 041406.